nature materials

Article

https://doi.org/10.1038/s41563-024-02090-w

Dynamic flow control through active matter programming language

Received: 10 November 2023

Accepted: 26 November 2024

Published online: 29 January 2025

Check for updates

Fan Yang[1,3] ✉, Shichen Liu[1,3], Heun Jin Lee[2], Rob Phillips[1,2] & Matt Thomson[1] ✉

Cells use 'active' energy-consuming motor and filament protein networks to control micrometre-scale transport and fluid flows. Biological active materials could be used in dynamically programmable devices that achieve spatial and temporal resolution that exceeds current microfluidic technologies. However, reconstituted motor–microtubule systems generate chaotic flows and cannot be directly harnessed for engineering applications. Here we develop a light-controlled programming strategy for biological active matter to construct micrometre-scale fluid flow fields for transport, separation and mixing. We circumvent nonlinear dynamic effects within the active fluids by limiting hydrodynamic interactions between contracting motor–filament networks patterned with light. Using a predictive model, we design and apply flow fields to accomplish canonical microfluidic tasks such as transporting and separating cell clusters, probing the extensional rheology of polymers and giant lipid vesicles and generating mixing flows at low Reynolds numbers. Our findings provide a framework for programming dynamic flows and demonstrate the potential of active matter systems as an engineering technology.

The control of micrometre-scale transport and fluid flow is a foundation of modern technology including synthetic chemistry, DNA sequencing and single-cell genomics[1,2]. Conventional transport control technologies including microfluidic devices generate force and flow at macroscopic length scales using pumps and vacuum manifolds, and then transmit force to microscopic length scales through channels that are fabricated in polydimethylsiloxane through soft lithography to control the fluid flows. Many of the challenges associated with micrometre-scale manipulation in conventional microfluidics stem from the fact that energy cascades down from macroscopic scales to microscopic scales. Specifically, flow fields generated by pumps are sculpted by passive channels fabricated for one task and cannot be dynamically reprogrammed for a new task. Furthermore, flow fields are shaped by channel geometry so that imperfections in design can lead to instabilities and intensive design and iteration cycles.

Biological systems achieve spatio-temporal control over fluid transport by inverting the flow of energy relative to current microfluidic technologies. Cells generate force and flow at molecular length scales through the hydrolysis of ATP by motor and filament proteins within 'active', energy-consuming, cytoskeletal structures[3]. Motor and filament proteins generate molecular-scale motion that then becomes organized on macroscopic, micrometre length scales through self-organization. By generating force on molecular length scales, cells can control the geometry of fluid flow fields with micrometre-scale precision for cell movement, internal transport and foraging[4–8]. Furthermore, cells can modulate the geometry of active structures in time to dynamically reprogram flow fields to respond to the environment.

Thus, biological active matter could provide a technology platform for the programming and dynamic control of fluids in technology applications, as decades of research has demonstrated that purified motor–filament proteins can generate micrometre-scale flows in solution[8–10]. Furthermore, the dynamics of active matter can be controlled with light proving a potential platform for optically programmable micrometre-scale transport[11]. Active-matter-based flow control could enable programmable execution of dynamic micrometre-scale tasks including transport, separation, sorting and mixing. However, a fundamental challenge is that active fluids are historically thought to be difficult to control and harness for applications because of the

[1]Division of Biology and Biological Engineering, California Institute of Technology, Pasadena, CA, USA. [2]Department of Applied Physics, California Institute of Technology, Pasadena, CA, USA. [3]These authors contributed equally: Fan Yang, Shichen Liu. ✉e-mail: fy2@caltech.edu; mthomson@caltech.edu

nonlinear active stresses and the coupling between active matter and solvent flows[10]. Specifically, previous work[10] demonstrates that active fluids can exhibit a phenomenon known as 'active turbulence', where generated flow fields exhibit vortices and other transient structures that have similarities to macroscopic turbulence. While active flows can be controlled through the fabrication of microfluidic chambers with designed boundaries[10], prefabricated geometries inherently limit the application of geometrically controlled active fluids and are not able to take advantage of or generate the dynamic spatio-temporal modulation of flows induced by active matter in biological systems[3,12]. Fundamentally, conceptual and theoretical paradigms that enable the control of active fluids could provide insight into the physical principles underlying the dynamics of force-generating active fluids.

Here we develop a spatio-temporally flexible programming paradigm for the modular design and construction of micrometre-scale flow fields using light-controlled biological active matter. We use an engineered system in which motor protein activity is modulated by light[11]. While in general the dynamics of the active fluids is nonlinear, we demonstrate a programming paradigm through which active-matter-powered flows can be composed through superposition to achieve a series of micrometre-scale transport, mixing and manipulating tasks. By composing 'primitive' flow fields generated by a single static or moving rectangular light bar, we are able to generate flow fields that enable the transport, stretching and separation of micrometre-scale particles. We apply superposition-based flow programming to generate flow fields for the extensional rheology of polymers and giant lipid vesicles (GVs), and for the micrometre-scale manipulation tasks on primary human cells, such as separating an unconstrained cell cluster into individual cells in situ. The advantages of our system are as follows: no requirements exist on precise channel design and microfabrication, polydimethylsiloxane lithography or pressure-pump control; our system can generate local flows around objects of interest without disturbing other regions in the channel; different programming modules can be additively assembled for specific transport tasks, enabling the streamlining of operations and multitasking in a single channel; and the system also allows us to move and control primary human cells, providing a potential platform for programmable manipulation of particles in biology and chemistry.

Flow programming through linear superposition of light bars

To harness the capabilities of biological active matter for technology applications, we seek to develop a modular framework where we can compose a basic set of primitive light patterns, such as rectangular bars, to generate flows that can achieve functions including transport, stretching and mixing. Our inspiration is Stokes flows, where inertial effects can be neglected and fluid dynamics can be described by a linear partial differential equation known as the Stokes equation: $\mu\nabla^2\mathbf{u} - \nabla p = \mathbf{0}$, with $\mathbf{u}$ the flow velocity, μ the viscosity and p the pressure. The amazing power of the dynamic linearity in Stokes flows is that, if we know the flow field generated by a single point source, then we can compose points sources, and the resulting flow field can be simply predicted through the addition of flow fields generated by these point forces individually[13]. Superposition provides a substantial simplification for predicting and programming flows through the simple addition of point sources. However, in our system we are sculpting flows using active-matter-generated forces, and in general, linear superposition does not hold for active fluids due to their inherent nonlinearity and apparent disorder[10,14].

Our experimental system consists of stabilized microtubules and kinesin motor proteins that have been engineered to reversibly 'link' in the presence of blue light by fusing motors to optically dimerizable improved light-induced dimer (iLID) proteins[11,15]. The kinesin K401 in our system is a homodimer that can bind on one microtubule in the dark state. Upon illumination with blue light, the kinesin motors form tetramers and can bind on two microtubules. To avoid confusion, we term the homodimer and tetramer motors 'unlinked' and 'linked' motors, respectively. In previous work[11], we demonstrated that light induction generates contractile motor–filament networks that induce spontaneous fluid flows within the system. In Supplementary Information, we formulate a continuum model that can quantitatively predict the dynamics of active matter and solvent flows. Our model is a three-phase complex fluids model, and the three phases are crosslinked microtubules, freely moving microtubules and solvent fluid. The crosslinked microtubules are modelled as a viscoelastic gel that self-contracts, driven by its internal active stresses; the freely moving microtubules are passive particles carried by both the gel and the solvent flow; and the solvent flow is generated by the contraction of the active gel and balanced by the hydrodynamic resistance in the flow cell (Supplementary Section I).

In our model, the solvent flow is governed by the Stokes equation with a driving force applied by the motion of crosslinked microtubules:

$$\gamma c(\mathbf{v} - \mathbf{u}) + \mu\nabla^2\mathbf{u} - \nabla p = \mathbf{0}, \tag{1}$$

where c and $\mathbf{v}$ are the spatially varying concentration and velocity of the crosslinked microtubules, respectively, and γ is the drag coefficient between the microtubules and the solvent. In equation (1), $\gamma c(\mathbf{v} - \mathbf{u})$ acts as a field of point forces applied upon the fluid. However, unlike the body-force-free Stokes equation, which is a purely linear, time-independent partial differential equation, active fluids are transient and nonlinear. Furthermore, the microtubule concentration field c is also carried by the solvent flow $\mathbf{u}$ (Supplementary Section I), so that the microtubule network at a position $\mathbf{r}_i$ experiences dynamics due to the long-range flows induced by the microtubule network at positions $\mathbf{r}_j$ in the system, where $\mathbf{r}$ is the position vector. In general c is therefore both time dependent and also an implicit function of the ambient flow field, $\mathbf{u}$. Fundamentally, the problem is that microtubule networks activated at different locations within the system interact through fluid flows, and flow-induced interactions lead to transport of the microtubule network, giving rise to nonlinear stresses and transport phenomena within the active fluids.

We find that superposition can be restored in the model by restricting interactions among spatially isolated regions of light signals. Mathematically, we show that the flow field $\mathbf{u}_i$ generated by a single network i decays as a power law $x^{-3.5}$ with x the distance to the bar centre. When another network j is placed beyond a cut-off distance such that $c_j\mathbf{u}_i = 0$ (Methods), superposition is recovered, and the flow field $\mathbf{u}$ generated by a system of spatially isolated light patterns can be predicted through simple linear superposition of individual forces in equation (1), that is, $\gamma c(\mathbf{v} - \mathbf{u}) = \gamma\sum_i c_i(\mathbf{v}_i - \mathbf{u}_i)$, where the subscript i indicates the microtubule concentration, velocity and solvent velocity, respectively, induced by a single network i, in the absence of other networks (Methods). This tells us that to maintain linearity in a system with multiple active agents at a low Reynolds number (Re), the flow fields induced by each agent should decay to be very small at the locations of other agents, as compared with their self-generated velocities. Therefore, we develop a modular programming strategy where we minimize long-range interactions by positioning the isolated light patterns far enough from each other so that the activated networks only weakly interact.

Superposition enables quantitative flow design

Consistent with our theory, we find experimentally that the flow field generated by two rectangular light bars can be predicted by superposition when the bars are separated above a critical spacing. We use a rectangular light bar as the basic unit of programming design, which dynamically functions as a microfluidic pump: the active network absorbs fluid lengthwise and pumps it out widthwise, generating four

https://doi.org/10.1038/s41563-024-02090-w

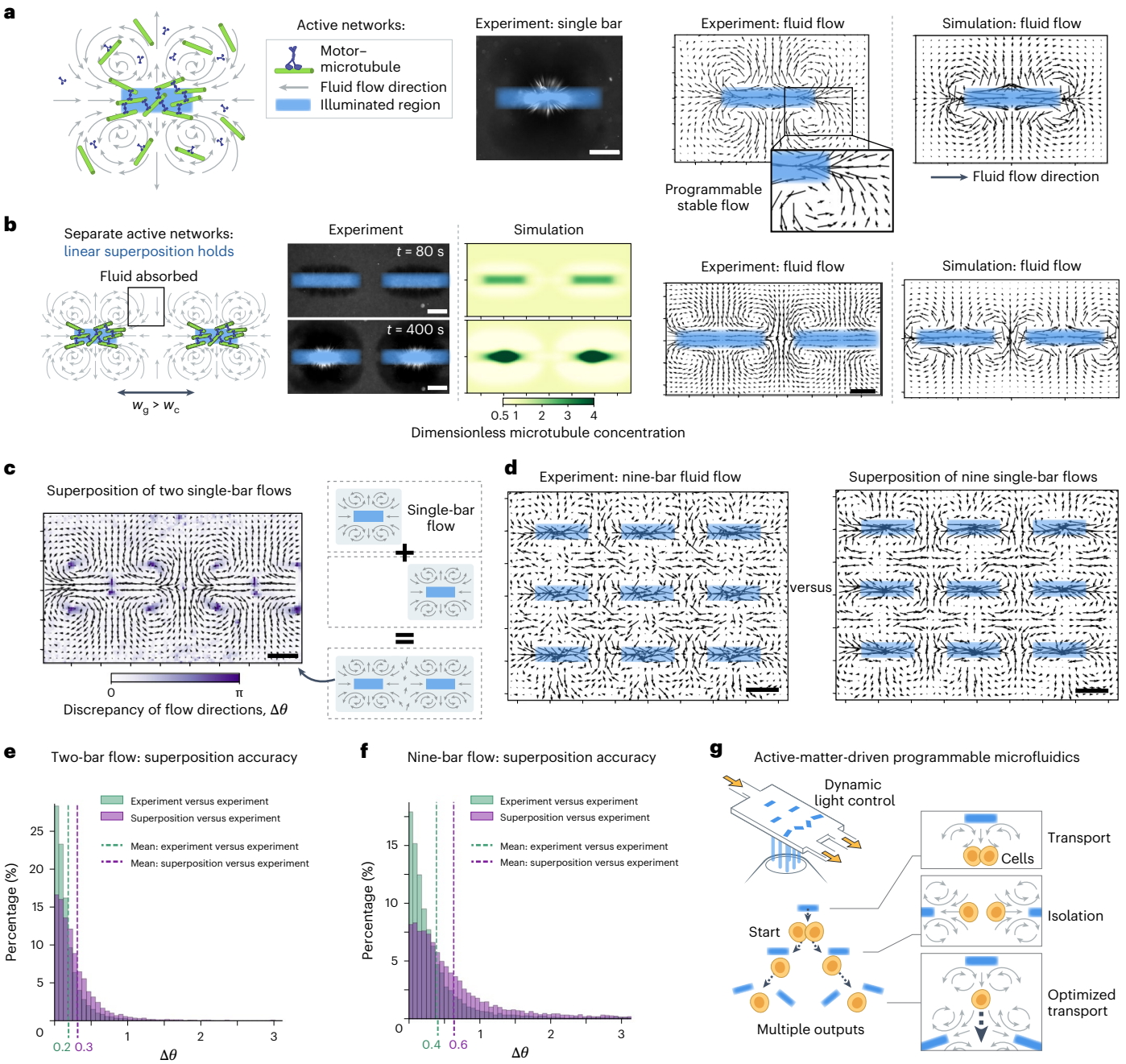

Fig. 1 | Linear superposition quantitatively predicts fluid flow fields induced by optically controlled active matter. a, A schematic (left) and an optical image (middle) of an active microtubule–motor network genterated by a single light bar, and its measured and simulated fluid flow fields (right). Under illumination, light-activatable motors can link to form tetramers and crosslink microtubules into a network (left). The contractile active network generates flows in the surrounding fluid, which is absorbed lengthwise into the light bar and pumped out widthwise (right). **b**, A schematic (left) and optical and simulated images (middle) of two active networks above the critical spacing, and their corresponding measured and simulated fluid flow fields (right). Above a critical spacing w_c, the flow field generated by two light bars is a linear superposition of two single-bar flows, as shown in **a**. **c**, Superposed flow fields from two experimental single-bar flows (left). The superposition process is sketched on the right. Comparison of the measured two-bar flow field with the superposition of two single-bar flows shows that the linear superposition holds quantitatively. The colour map (left) represents the angle $\Delta\theta \in [0, \pi]$ between the measured and superposed flows. **d**, Measured nine-bar flow fields and superposition of nine single-bar flows to assemble a nine-bar-array flow. **e**,**f**, Superposition provides high-accuracy flow field prediction for both two-bar (**e**) and nine-bar (**f**) compositions, with errors comparable to variations in experimental replicates. **g**, Linear superposition enables construction of active-matter-driven programmable microfluidics. The sketch shows a conceptual application using an assembly of light bars to transport and separate cells. All scale bars are 100 μm and all flow fields are time-averaged over 240 s.

counter-rotating vortices (Fig. 1a). We test our principle for linear superposition with two light bars placed side by side. When their gap width w_g exceeds a critical spacing w_c, the active networks self-contract within their respective illuminated regions (Fig. 1b). The resultant microtubule and flow fields (Fig. 1b) are, at least qualitatively, a linear superposition of two single-bar fields (Fig. 1a).

We find that the linear superposition of single-bar flows can quantitatively predict flow fields generated by multi-bar compositions.

https://doi.org/10.1038/s41563-024-02090-w

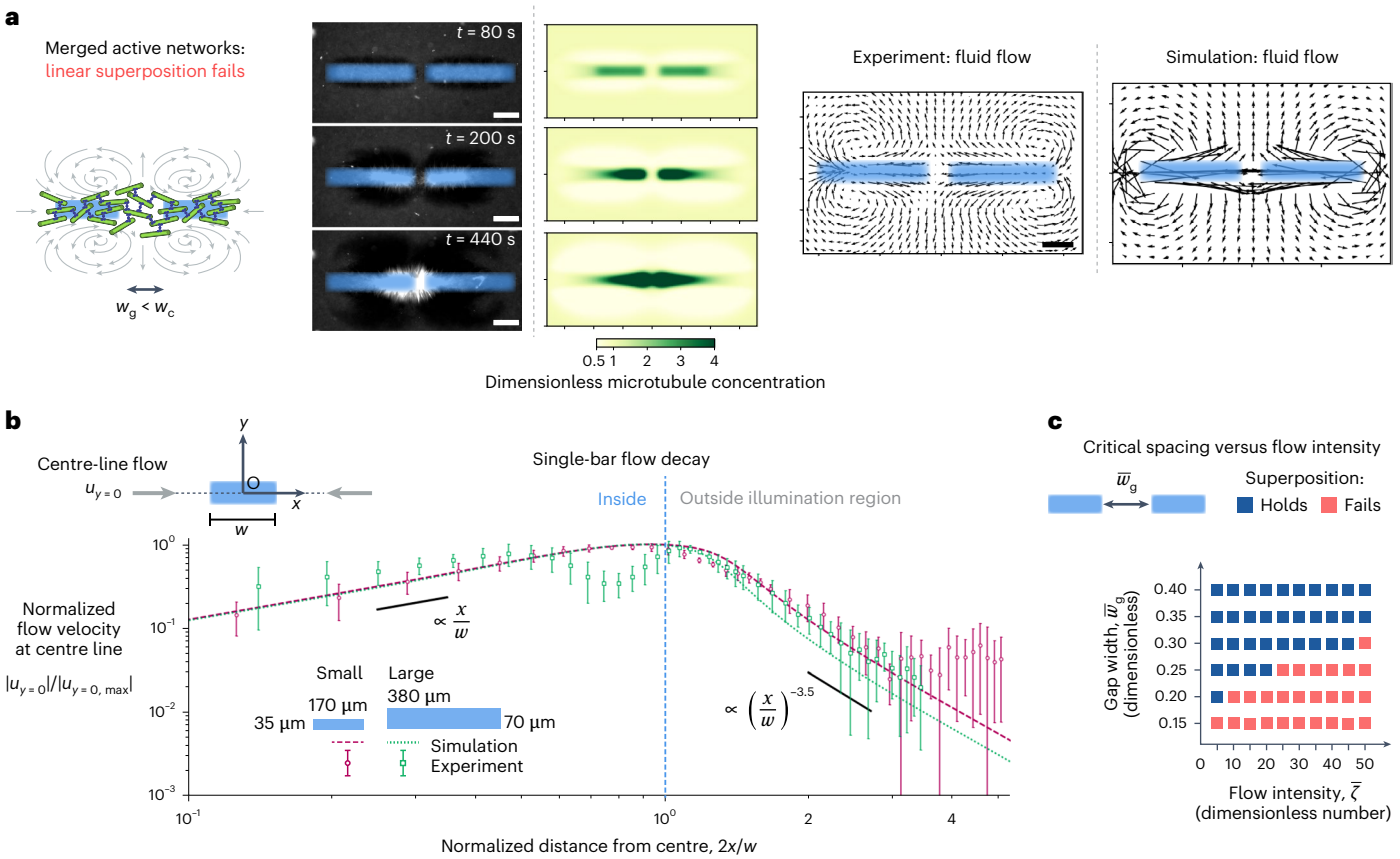

Fig. 2 | Superposition length scale is set by hydrodynamic interactions between active networks. a, A schematic (left) and optical and simulated images (middle) of two active networks below the critical spacing, and their corresponding measured and simulated fluid flow fields (right). The simulated microtubule concentration is normalized by its initial value. Below the critical spacing, linear superposition of flow fields fails. The active networks move towards each other and eventually merge. Scale bars, 100 μm. **b**, The centre-line flow profile induced by a single bar. $u_{y=0}$ is the fluid flow at the centre line $y = 0$ of the light bar as shown in the top-left diagram, where O is the centre of the light bar. $u_{y=0,max}$ is the maximum centre-line flow speed. The flow magnitude grows linearly as x/w and decays as $(x/w)^{-3.5}$ inside and oustide the illumination region, respectively. Data are presented as mean values ± s.d. of eight experiments. **c**, Simulated phase diagram of superposition shows that the critical spacing increases with the fluid flow intensity. All flow fields are averaged over 240 s.

We additively assemble the single-bar flow fields (Fig. 1a) to construct two-bar (Fig. 1c) and nine-bar (Fig. 1d) fluid flows, and plot the discrepancy of flow directions with measured flows in Fig. 1e,f, respectively. Two main sources of discrepancy exist: (1) the errors induced by superposition and (2) the experimental variations from inherent thermal fluctuations and variations in concentration and activity of the proteins during the preparation process in independent experiments. To distinguish between them, we compare the distributions of discrepancy from superposition with the distributions of experimental variations (Fig. 1e,f), which shows that the errors induced by superposition are comparable to the intrinsic experimental variations. Similarly we also compare the discrepancy of flow magnitudes in the superposition of two-bar flows with experimental variations (Supplementary Fig. 7). The mean fractional change of magnitudes induced by superposition is 0.31, only slightly above the mean in experimental variations, which is 0.23. The small superposition-induced errors in both flow magnitudes and directions demonstrate that linear superposition can be achieved quantitatively in multi-bar compositions. Linear superposition has long been thought to be impossible in active matter systems, but in our experiments it is made possible by confining the active matter within the illuminated regions. Outside the light regions, microtubules and unlinked motors do not crosslink, and the dynamic linearity of Stokes flows still holds. Linear superposition is the foundation of constructing a modular programming language for microfluidic control (Fig. 1g). In our control strategy, only fluid flows outside the illuminated regions are used for transport tasks (Fig. 1g).

Hydrodynamic interactions set superposition length scales

The linear superposition fails when the spacing between light bars is below a critical length. The active networks move outside the light regions and eventually merge (Fig. 2a). Our continuum model allows us to determine how the critical spacing originates from hydrodynamic interactions between active networks. The rectangular active networks absorb fluid flow along the long axis (x axis in Fig. 2b) and therefore can attract neighbouring networks through hydrodynamic interactions. The flow decaying with distance provides a mechanism for whether the two active networks will merge. In the two-bar composition (Figs. 1b and 2a), each network generates flow that propagates to the neighbouring network. The flow field generated by one network, therefore, exerts force on the neighbouring network, leading to flow-induced drift that is also counteracted by activity-induced self-contraction. When bars are placed close enough, within a critical length w_c, the flow generated by one network is sufficient to move the other network out of the illumination region, in spite of the self-contraction (Fig. 2a).

How flow decays with the distance to the bar centre is essential in determining the critical spacing, which is found to follow a power law. The intensity of a flow field generated by a given rectangular network determines the network spacing required for superposition to hold. We first conduct simulations and experiments with two light bars of different sizes and similar aspect ratios (Fig. 2b). The scaling of the flow magnitude is the same for both bars, and grows linearly and decays as $(x/w)^{-3.5}$ within and outside the illuminated region, respectively, where

w is the bar length. The simulations are in quantitative agreement with experiments, except for a small region near the edge of the larger light bar. The flow magnitude drops slightly in this region, which may suggest that a boundary layer develops here when the light bar is large enough. The flow data for two sizes of bars collapse onto each other when the distance x is normalized by the bar length w (Fig. 2b), demonstrating that w is the length scale of flow variation. In practice, a spacing of half of the bar length $w/2$ is usually enough to avoid the merging of networks, as the flow already decays by more than 98% at $x = 3w/2$. Note that the estimate $w_c \approx w/2$ shows that the critical distance grows linearly with the bar length. However, the factor 1/2 is an overestimate and can guarantee linear superposition in a wide range of bar scales and aspect ratios in practice. The exact values of w_c also depend on the flow conditions, such as the solvent viscosity and the flow chamber height, as discussed below. To test the generality of superposition, we also compute the effects of aspect ratios of light bars on the flow decay. Numerical results reveal that the flows outside the illuminated regions always decay in a power law, with the exponents ranging from −4 to −3.5, regardless of the aspect ratios (Supplementary Fig. 2). This demonstrates that linear superposition can be generalized to different bar sizes and shapes. Additionally, we perform a superposition of experimental flow fields generated by pentagonal light patterns in Supplementary Fig. 8 to show that the principle of linear superposition is not limited to rectangular light shapes.

To test how the flow intensity affects the critical spacing, we compute a phase diagram of two networks with different gap widths and flow intensities (Fig. 2c). The flow intensity is tuned by a dimensionless parameter $\bar{\zeta} = c_0\gamma h^2/12\mu$, where c_0 is the initial microtubule concentration and h is the height of the flow cell. The parameter $\bar{\zeta}$ is found to be the most important dimensionless number governing the flow intensity in our model (Supplementary Information equation (28)). The physical meaning of $\bar{\zeta}$ is the ratio of the driving force, $c_0\gamma$, and the hydrodynamic resistance in the flow cell, $12\mu/h^2$. The phase diagram (Fig. 2c) shows that the critical spacing required for superposition increases with the flow intensity. The reason is that as the flow intensity generated by network one increases, network two, its neighbouring network, should be placed farther away. This ensures that the flow induced by network one decays to be no longer sufficient to drag network two outside the illuminated region.

Optimized transport

Superposition opens up a convenient route to the design of flow fields using optimization via translation, rotation and summation of single-bar flow data. We study an optimization problem of using three light bars to transport particles along a line segment AB (Fig. 3a). The objective function f is defined as the line integral of fluid flows along AB (Fig. 3a). To ensure the particle transport along a straight path, the line segment AB should be placed at the axis of symmetry of the bar configurations (Fig. 3b). Using simulated flow data, we can plot the optimization landscape (Fig. 3c). Each point in Fig. 3c is already optimized over the orientation angle (Supplementary Section III). The optimal solution, consisting of the optimal x and y coordinates and the optimal orientation angle of each light bar, can be found by the maximum value in the optimization landscape, labelled by a star in Fig. 3c. We test this optimal solution in experiments by comparison with non-optimal three-bar configurations, and find that the optimal solution transports particles both fastest and furthest (Fig. 3d,e). The results show that the active matter programming language is capable of optimizing practical design using only the linear transformation of single-bar flow fields.

Programming flows for microrheology and cell isolation

To show that the active matter programming language can be flexibly applied and motivate new applications, we use stretching flows induced by two light bars (Fig. 3f) for the microrheology of polymers, division of GVs and manipulation tasks of cells. The rheological properties of polymer networks can be inferred from their deformation parameter $\mathrm{DF} = (L - B)/(L + B)$ and flow strain rates in an extensional flow, where L and B are the length and breadth of the deformed aster, respectively (Fig. 3g). We use the two-bar flow to stretch a microtubule aster preformed with a circular light pattern (Fig. 3g). Measurement of strain rates at the gap centre shows that the flow is quasi-steady beginning at time $t = 100$ s, and the average value is $\partial u_x/\partial x \approx 0.0015\ \mathrm{s}^{-1}$, where u_x is the flow speed in the x direction (Fig. 3g). Consequently the shear modulus of the microtubule aster is calculated to be 1×10^{-7} Pa (Methods). This shows that our system can potentially be used in extensional rheology where viscoelastic properties of materials are deduced from their deformation profiles under straining[16], and also in single polymer dynamics[17] where single polymers, such as DNA strands[18], need to be stretched in situ. To perform these functions, traditional microfluidics usually relies on the channel geometry to generate stretching flows[19], such as sculpting a channel contraction[20,21] or cross-slot geometries[18]. However the former geometry cannot fix particles in the channel because the flow will constantly carry them downstream; the cross-slot or Taylor's four-mill geometries[22] can fix the particle at an equilibrium point but it is difficult to move the particle to this point since it is mechanically unstable. By contrast, the active matter programming language can be flexibly implemented to stretch particles in situ, by projecting light patterns around objects of interest. Our method is not meant to replace state-of-the-art high-end methods like optical tweezers but provides a low-cost and simple strategy for microrheology.

To further demonstrate the versatility of our system in extensional rheology, we demonstrate using the stretching module to stretch and divide a GV into daughter vesicles in Extended Data Fig. 1 and Supplementary Video 3. GVs are extensively studied as the basic model for artificial cells[23]. Division of GVs can be used to probe their mechanical properties and is also crucial to mimic cell division[24]. At the initial stage ($t \leq 88$ s), we observe the fusion of two giant unilamellar vesicles (GUVs) and an oligovesicular vesicle (OVV) into a larger GV (Extended Data Fig. 1b). OVVs represent the structure of 'vesicles in vesicle'[25] and are common by-products during GV preparation[26] (Methods). The solvent flow is relatively small at the initial stage (Supplementary Fig. 4) and the mechanism of GV fusion is unclear to us. The fused GV then undergoes

Fig. 3 | Superposition provides a simple design principle for optimized transport of particles, microrheology of polymers and isolation of cells. **a**, The design goal, to move a particle from point A to point B (left), and its corresponding objective function (right). **b**, The particle path AB should coincide with the axis of symmetry in the composition of light bars. **c**, The optimal three-bar configuration is determined by the maximum value in the optimization landscape (left) and displayed on the right. **d**, Experimental images of using the optimal light bar configuration (blue) to transport two particles. **e**, Time course of particle displacement in optimal versus non-optimal designs. **f**, Measured and simulated stretching flows generated by two light bars (left) and their quantitative discrepancy (right). Both flow fields are averaged over 240 s. **g**, Schematic (top) and experimental images (bottom) of a preformed microtubule aster being stretched by the elongational flow, which is used to measure rheological properties of the aster (i). Measured flow strain rates over time in the polymer-stretching and cell-separating experiments (ii). The strain rates are averaged over a 140 μm × 50 μm region at the gap centre. Data are presented by mean values ± s.d. of four experiments. **h**, Schematic (top) and snapshots (bottom) of detaching two cells (i). Centre-to-centre distance of the two cells and estimated detachment force over time (ii). **i**, Schematic (top) and snapshots (bottom) of separation of a cell cluster in the stretching flow (i). Centre-to-centre distances of cells over time (ii). Due to constraints of image resolution, the time of detachment has an error of ±30 s. The scale bars are 100 μm in **d** and **g** and 20 μm in **h** and **i**.

https://doi.org/10.1038/s41563-024-02090-w

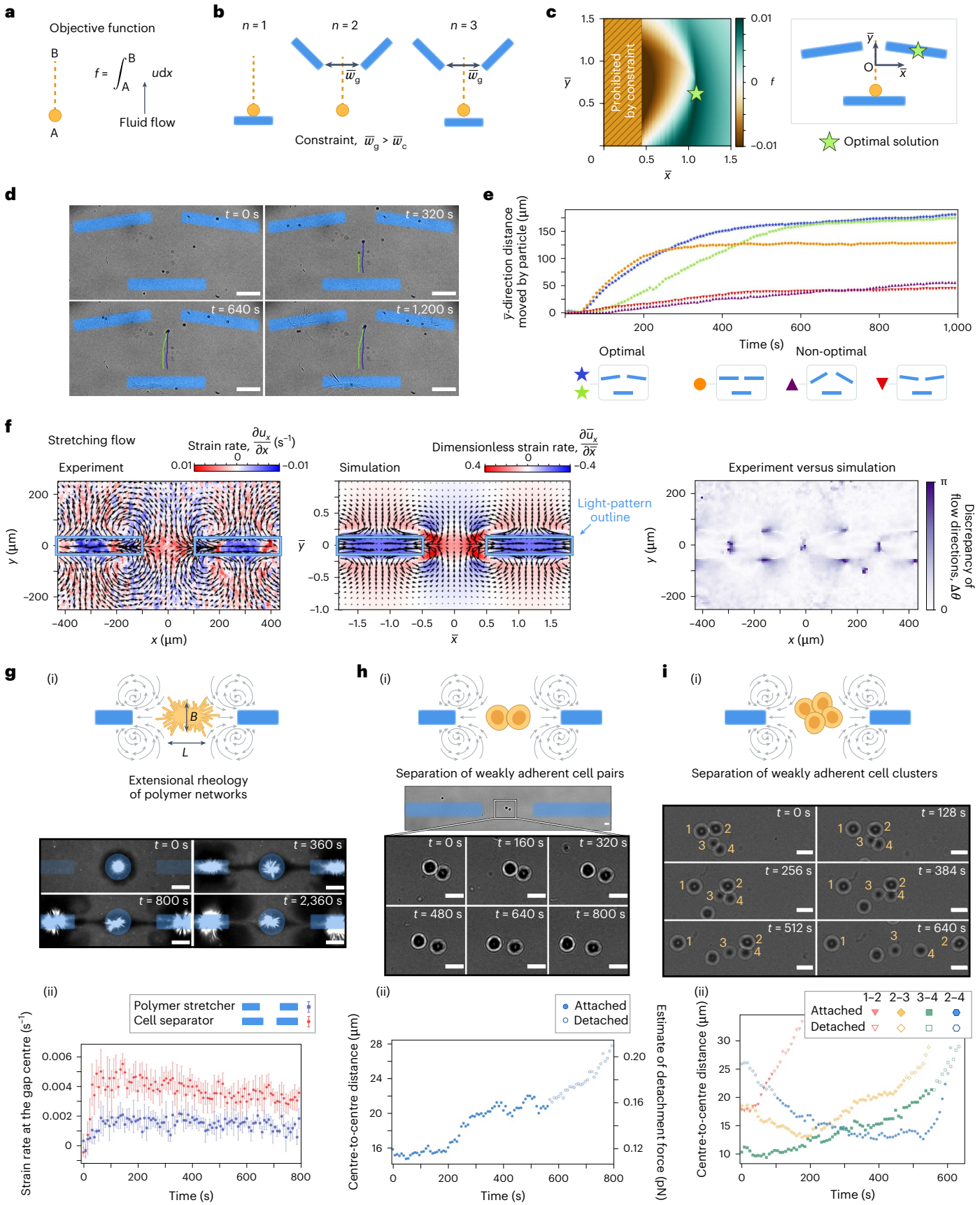

stretching due to the flow and becomes elongated along the axis of the maximum strain rate (Extended Data Fig. 1c). Between $t = 584$ s and 616 s, the GV is divided into three daughter vesicles (Extended Data Fig. 1d). The daughter vesicles are stable in the solvent flow (Extended Data Fig. 1e).

We now demonstrate using active matter to separate an unconstrained, weakly adherent cell cluster into isolated cells. Separation of cells is central in cell sorting applications[27]. Systematic study of cell–cell detachment is usually conducted through either atomic force microscopy (AFM)[28] or by pulling two cells apart using two micropipettes[29,30]. Both methods require highly skilled operators and also could harm the cells when constraining them with solid instruments. By contrast, our system can generate extensional flows in the vicinity of cell clusters and separate them (Fig. 3h and Supplementary Video 1). The cells used are Jurkat cells, which are a human T cell line and known to express cell adhesion molecules such as integrins and CD2 receptors[31,32]. The local flow strain rates near the cells are around 0.004 s^{-1} (Fig. 3g), and the application of flows for 500–800 s leads to cell detachment. The detachment force applied by the flow is approximately $3\pi\mu a\Delta l\partial u_x/\partial x$ (Methods), where $a = 10$ μm is the cell radius, and Δl is the centre-to-centre distance of the cell pair (Fig. 3h). Using the average strain rate 0.004 s^{-1}, the detachment force is proportional to Δl and calculated in Fig. 3h. The detachment force generated in our set-up, around 0.1 pN, is much smaller than the adhesion force measured by AFM on Jurkat cells, at the scale of 10 pN. This suggests that strong adhesive bonds are not formed in the cell pair in Fig. 3h and the cells have the morphology of weakly adherent cells with surface interactions but not cortical associations[33,34]. To confirm whether our set-up can separate strongly adherent cells and also to test the viability of cells in the solution, we stain the cells with viability indicators, ethidium homodimer-1 (EthD-1) for dead cells and calcein AM for live cells, as shown in Extended Data Fig. 2. We find that both Jurkat and Raji cells (Methods) can stay alive in our solution, but the stretching module cannot separate live-cell clusters, due to the weak force that it can provide. This confirms that our set-up can separate only weakly adherent cells. However, this 'small force' generated by the stretching module can be used for applications such as isolating dead cells from live cells. In Extended Data Fig. 2a, we isolate one live cell from a dead-cell pair that are initially close with each other, at a distance of 30 μm. Both the live and dead cells follow the solvent flow and move in opposite directions. In Extended Data Fig. 2b, we demonstrate isolating a pair of dead cells from a cluster of at least seven live cells, initially separated by 20 μm. The dead cells move to the left while the live-cell cluster is undisturbed because it is too big to be transported by the flow. These examples demonstrate that the small-force feature of our set-up can also be used to separate weakly adherent cells from strongly adherent cell clusters at the micrometre scale.

Weakly adherent cell clusters consisting of more than two cells can also be separated in situ, revealing more complex collective behaviours. Figure 3i and Supplementary Video 2 show the separation of a four-cell cluster in the extensional flow. In addition to three cell–cell separation events (1–2, 2–3 and 3–4 in Fig. 3i), we also observed two initially separated cells (2 and 4 in Fig. 3i) first coming into contact and then being separated, through sliding along the membrane of cell 3. New applications like these can be motivated by our system because our system allows for the flexible sculpting of local flow fields near particles of interest, as opposed to traditional microfluidics, which usually relies on pumps to generate a global flow throughout the entire channel.

Active mixing with rotating bars

Our programming framework can also be extended to dynamic light patterns. Mixing at low Re is a major challenge in microfluidics because flows are laminar in this regime and molecular diffusion is slow[35]. We show that a rotating light bar can generate stirring flows to mix the circular region swept by it. Both the crosslinked microtubule gel and the flow field, consisting of four vortices, rotate following the rotating light bar, as shown in Fig. 4a,b, which can also be predicted by our simulations. As the light bar rotates, the microtubule gel dynamically forms and self-contracts into a core. As the light bar is shed on a new location from one pulse to the next, two plumes of newly crosslinked microtubules are formed at the ends of the gel, which transport both the mass and momentum of the microtubules to the network core, as well as rotating the more densely crosslinked network centre (Fig. 4a). After one cycle, the circular region swept by the light bar will be mixed by the rotating vortices (Fig. 4b).

We quantify the mixing efficiency of the active mixer made from a rotating bar on fluorescent particles, and find a tenfold increase in mixing efficiency comparing with the passive mixing by pure diffusion (Fig. 4c,d). The active mixing is mainly accomplished by three flow effects at different length scales. At the length scale of the light bar, w, the rotating bar can push particles from one side of the interface to the other. At the length scale of the vortices, $w/2$, each region occupied by one of the four vortices is mixed by the vortex. At the length scale of the thermal motions of the active microtubules, the small-scale flows can also help randomly mix the particles[10]. To quantify the mixing efficiency at all length scales, we adopt a multi-scale mix-norm[36]. For a particle fluorescence intensity field $I(\mathbf{r}, t)$ with a Fourier expansion, $I(\mathbf{r}, t) = \sum_{\mathbf{k}} I_{\mathbf{k}} e^{i2\pi\mathbf{k}\cdot\mathbf{r}}$, where $\mathbf{k}$ and $I_{\mathbf{k}}$ are the wave vector and its corresponding Fourier coefficient, respectively, and i is the unit imaginary number. The norm is defined by $\| I(\mathbf{r}, t)\| = \left(\sum_{\mathbf{k}\neq 0} |\mathbf{k}|^{-2} |I_{\mathbf{k}}|^2\right)^{1/2}$ (ref. 36). We further rescale $\|I(\boldsymbol{r}, t)\|$ by its initial value, and define the mix-norm to be $\|I(\mathbf{r}, t)\|/\|I(\mathbf{r}, t = 0)\|$. A lower mix-norm represents a better mixing result. The time courses of mix-norms in passive and active mixing are plotted in Fig. 4d. At $t = 800$ s, the mix-norms in active and passive mixing drop 22% and 2%, respectively, which demonstrates that active mixing is tenfold more effective than passive mixing by diffusion. Another advantage of our system is that it can create localized mixing in a designated region without disturbing its surroundings. The size and location of the mixing region can be programmatically controlled by optical signals. Mixing is notoriously difficult in microfluidics, where current techniques usually require textured surfaces[35] or external energy input[37] to stir the flow. The stirring flows then need to pass through a long channel to ensure enough time for mixing. Our system provides a promising method for locally mixing arbitrary regions without passage through a long channel.

Multi-step flow programs designed by superposition

Superposition enables the assembly of programming modules in space and time to streamline multi-step tasks. We first show a module combination to transport and separate cells at the same time (Fig. 5a). The cells are propelled by the outflow generated by the bottom bar, and isolated by the two bars at the top. The flow fields can be easily predicted from the linear superposition of simulated single-bar flow data (Fig. 5a), which can also be used to adjust the bar positions and inclinations. For example, we design the two top bars to tilt downward to facilitate the cell transport. Experiments verify that the module combination can transport and isolate cells at the same time (Fig. 5b,c).

We also sequence two dynamic light signals in time to transport and mix particles at a larger scale (Fig. 5d). We first transport the particles from right to left using three translating bars. The inflows of light bars can attract particles that form into three stripes following the bars' movement. We then use three rotating bars to mix the stripes of particles, which disperse in the region originally devoid of particles.

Discussion

In this paper, we harness biological active matter for engineering applications, opening the way for a broad range of active-matter-powered devices and providing a paradigm for flow control and materials

https://doi.org/10.1038/s41563-024-02090-w

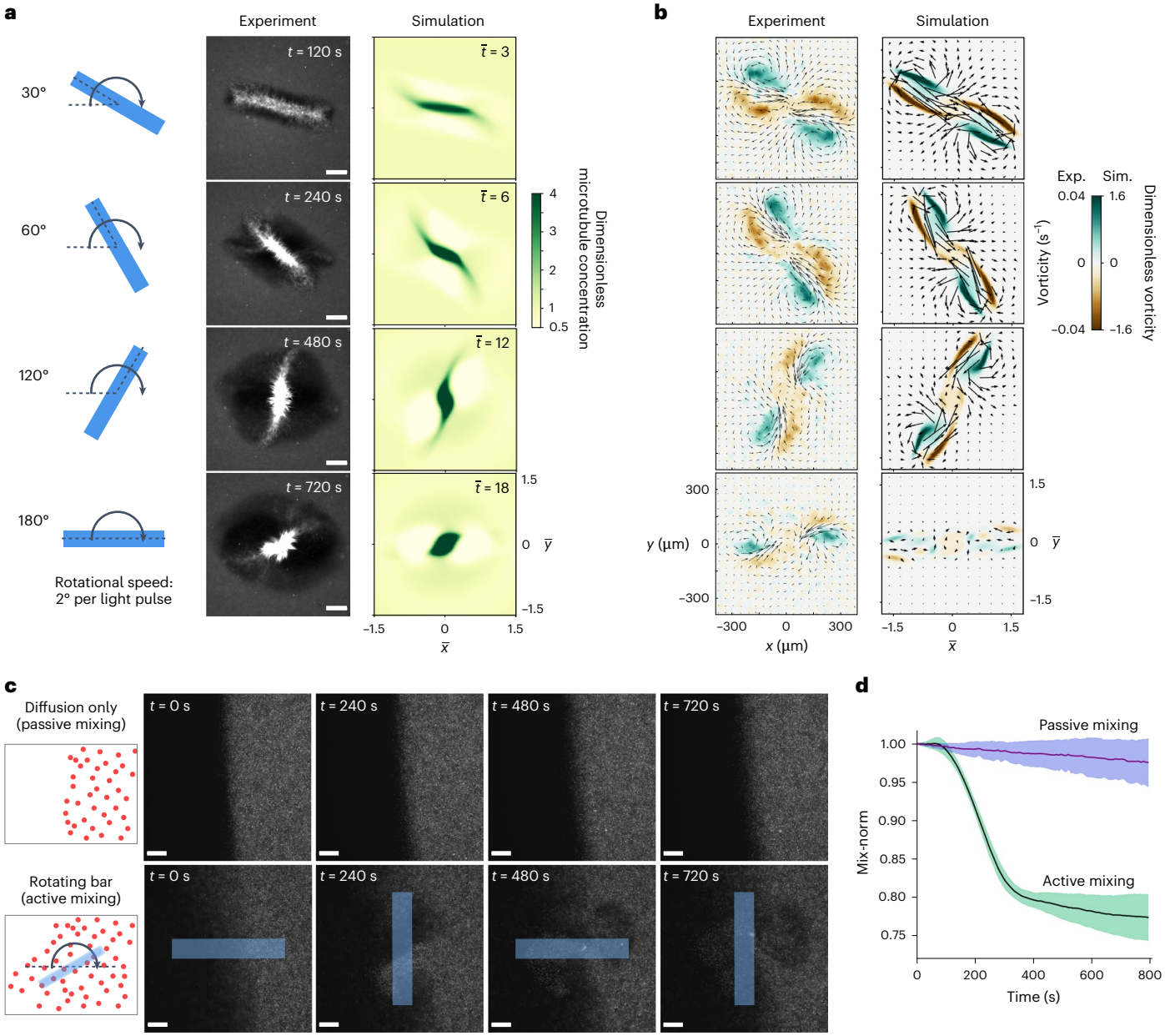

Fig. 4 | Rotating light bars enable active mixing in microfluidics. **a**, Experimental and simulated images of microtubules under a rotating light bar, shown at the left. **b**, Measured (Exp.) and simulated (Sim.) flow fields in **a**. The colour map shows the flow vorticity. The measured flow fields are averaged over five experiments. **c**, A rotating bar can mix particles in the circular region swept by it, as shown in the left diagrams. The controlled experiment on the top shows that passive mixing by diffusion is much weaker than this active mixing. **d**, Time courses of mix-norms in active and passive mixing. Data are presented as mean values ± s.d. of five experiments. All scale bars, 100 μm.

science. Active materials generate force at molecular scales and can be exploited as a hardware in technology[38], but systematic control of active matter has been a challenge. Here we demonstrate a pathway by modulating the active-matter motions with a programmable external field, light. Furthermore, the dynamics of active fluids can be quantitatively predicted by a continuum model, and a model-driven design and optimization of flow fields are realized.

The linear superposition of local coherent flows allows for the methodical design of complex flow fields and the scale-up of our system. While active fluids are generally thought to be chaotic and difficult to control, we find that the nonlinear interactions of active networks decay as a power law with their separation length. This leads to a programming principle where we first construct local regions of organized flows and then isolate them above a critical spacing so that the networks are weakly interacting and the local flow fields can be additively assembled in the entire channel. Our modular programming strategies also provide theoretical insights into how to maintain order and perform work in active fluids. Our theory gives a general framework for microtubule–motor–solvent systems, which may be extended to study other out-of-equilibrium structures of the cytoskeleton, such as mitotic spindles. All experiments in this paper were controlled to be at similar conditions and all simulations shared the same physical parameters, demonstrating the versatility of our model.

Our platform can be developed towards building a universal single device that can integrate and automate diverse micrometre-scale transport tasks in a single channel, and will motivate numerous applications in chemistry and biology. Further improvements to our system include expanding the toolbox of basic flow units for more adaptable

https://doi.org/10.1038/s41563-024-02090-w

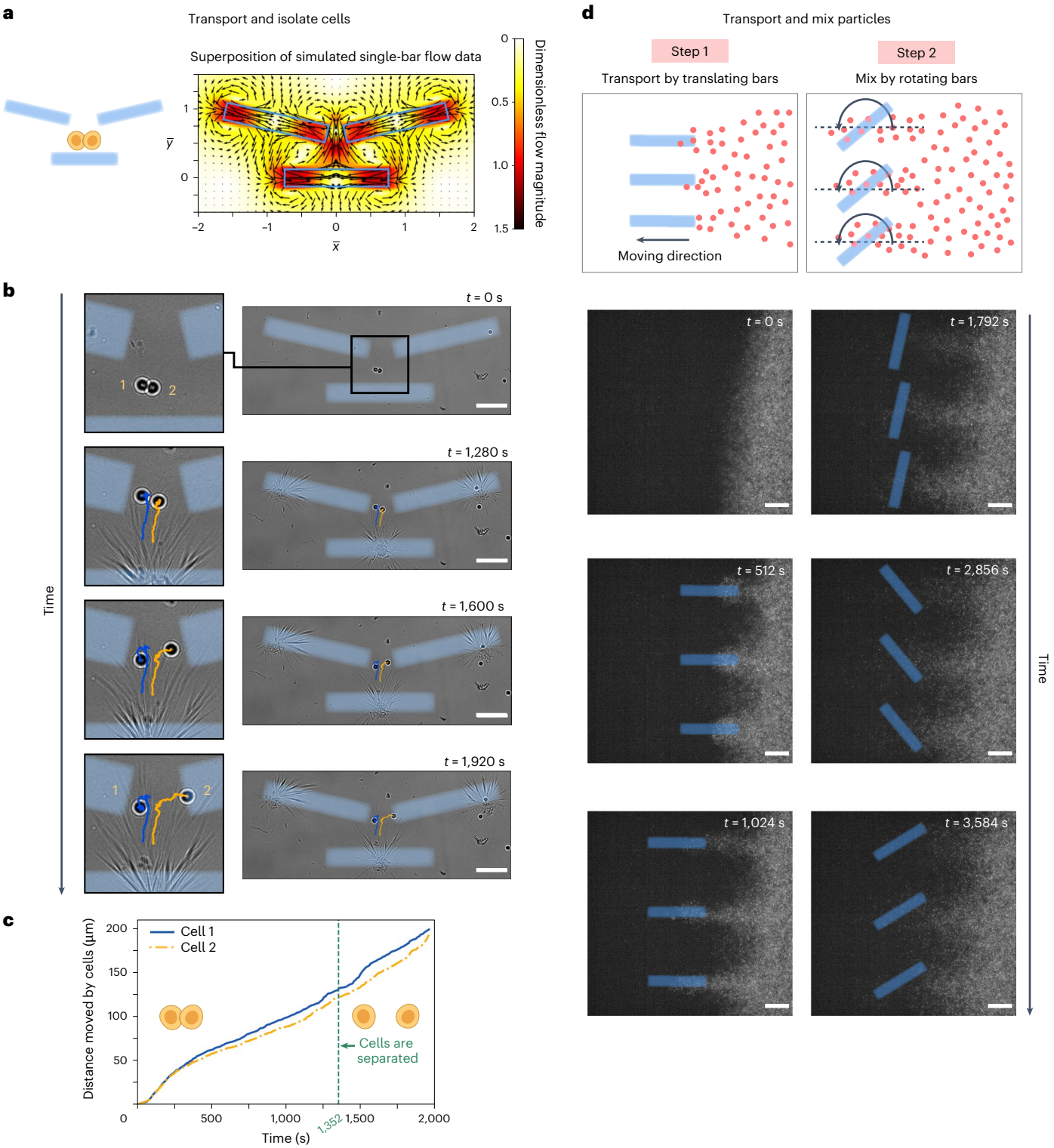

Fig. 5 | Programming modules can be additively assembled in space and time to streamline multi-step tasks. a, Combination of transporting and stretching modules, shown in the schematic at the left, can be designed from the superposition of single-bar flow data. **b**, Experimental images of transporting and isolating cells at the same time. **c**, The distance travelled by the cells over time, with cells shown in schematics. **d**, Schematics (top) and experimental images (bottom) of transporting and mixing particles by sequencing dynamic light signals in time. All scale bars, 100 μm.

flow design, by incorporating flow fields generated from different light shapes, such as polygons, ellipses and concave shapes. Our set-up could also be developed into a closed-loop control system by integrating a computer-vision program to analyse the images of the channel, and a decision-making program to compute the optical input based on real-time feedback and task goals. To overcome limitations in the proteins' sensitivity towards temperature and solute conditions, we are extending our current system to build a double-layer structure, where the top layer contains the solvent and objects of interest and the bottom layer is the active fluids. The two layers are immiscible and the idea is

to program the flow in the bottom layer, which in turn will control the motion of the top layer through force transmission at the interface.

Interest has been growing in using optical control as a non-invasive method to generate micrometre-scale flows. Laser-induced heat has been shown to generate a thermoviscous flow inside embryos, which can be applied to probe the biological functions of cytoplasmic flows and active microrheology in cells[39]. An electrically programmable microfluidic device has been proposed recently using artificial cilia to stir flows near chamber walls[40]; our set-up is more efficient in driving flows near the centre. Different programmable control mechanisms might complement each other towards a fully automated future of microfluidics.

Online content

Any methods, additional references, Nature Portfolio reporting summaries, source data, extended data, supplementary information, acknowledgements, peer review information; details of author contributions and competing interests; and statements of data and code availability are available at https://doi.org/10.1038/s41563-024-02090-w.

References

1. Stone, H. A., Stroock, A. D. & Ajdari, A. Engineering flows in small devices: microfluidics toward a lab-on-a-chip. *Annu. Rev. Fluid Mech.* **36**, 381–411 (2004).
2. Whitesides, G. M. The origins and the future of microfluidics. *Nature* **442**, 368–373 (2006).
3. Gilpin, W., Prakash, V. N. & Prakash, M. Vortex arrays and ciliary tangles underlie the feeding–swimming trade-off in starfish larvae. *Nat. Phys.* **13**, 380–386 (2017).
4. Kamiya, N. Physical and chemical basis of cytoplasmic streaming. *Ann. Rev. Plant Physiol.* **32**, 205–236 (1981).
5. Glotzer, J. B., Saffrich, R., Glotzer, M. & Ephrussi, A. Cytoplasmic flows localize injected oskar RNA in *Drosophila* oocytes. *Curr. Biol.* **7**, 326–337 (1997).
6. Forrest, K. M. & Gavis, E. R. Live imaging of endogenous RNA reveals a diffusion and entrapment mechanism for *nanos* mRNA localization in *Drosophila*. *Curr. Biol.* **13**, 1159–1168 (2003).
7. Needleman, D. & Shelley, M. J. The stormy fluid dynamics of the living cell. *Phys. Today* **72**, 32–38 (2019).
8. Stein, D. B., De Canio, G., Lauga, E., Shelley, M. J. & Goldstein, R. E. Swirling instability of the microtubule cytoskeleton. *Phys. Rev. Lett.* **126**, 028103 (2021).
9. Suzuki, K., Miyazaki, M., Takagi, J., Itabashi, T. & Ishiwata, S. Spatial confinement of active microtubule networks induces large-scale rotational cytoplasmic flow. *Proc. Natl Acad. Sci. USA* **114**, 2922–2927 (2017).
10. Wu, K. T. et al. Transition from turbulent to coherent flows in confined three-dimensional active fluids. *Science* **355**, eaal1979 (2017).
11. Ross, T. D. et al. Controlling organization and forces in active matter through optically defined boundaries. *Nature* **572**, 224–229 (2019).
12. Mathijssen, A. J. T. M., Culver, J., Bhamla, M. S. & Prakash, M. Collective intercellular communication through ultra-fast hydrodynamic trigger waves. *Nature* **571**, 560–564 (2019).
13. Leal, L. G. *Advanced Transport Phenomena* (Cambridge Univ. Press, 2007).
14. Marchetti, M. C. et al. Hydrodynamics of soft active matter. *Rev. Mod. Phys.* **85**, 1143–1189 (2013).
15. Guntas, G., Hallett, R. A., Zimmerman, S. P. & Kuhlman, B. Engineering an improved light-induced dimer (iLID) for controlling the localization and activity of signaling proteins. *Proc. Natl Acad. Sci. USA* **112**, 112–117 (2015).
16. Squires, T. M. & Mason, T. G. Fluid mechanics of microrheology. *Annu. Rev. Fluid Mech.* **42**, 413–438 (2010).
17. Schroeder, C. M. Single polymer dynamics for molecular rheology. *J. Rheol.* **62**, 371–403 (2018).
18. Perkins, T. T., Smith, D. E. & Chu, S. Single polymer dynamics in an elongational flow. *Science* **276**, 2016–2021 (1997).
19. Foster, K. M., Papavassiliou, D. V. & O'Rear, E. A. Elongational stresses and cells. *Cells* **10**, 2352 (2021).
20. Ober, T. J., Haward, S. J., Pipe, C. J., Soulages, J. & Mckinley, G. H. Microfluidic extensional rheometry using a hyperbolic contraction geometry. *Rheol. Acta* **52**, 529–546 (2013).
21. Mancuso, J. E. & Ristenpart, W. D. Stretching of red blood cells at high strain rates. *Phys. Rev. Fluids* **2**, 101101 (2017).
22. Taylor, G. I. The formation of emulsions in definable fields of flow. *Proc. Math. Phys. Eng.* **146**, 501–523 (1934).
23. Walde, P., Cosentino, K., Engel, H. & Stano, P. Giant vesicles: preparations and applications. *ChemBioChem* **11**, 848–865 (2010).
24. Miele, Y., Holló, G., Lagzi, I. & Rossi, F. Shape deformation, budding and division of giant vesicles and artificial cells: a review. *Life* **12**, 841–865 (2022).
25. Šegota, S. Spontaneous formation of vesicles. *Adv. Colloid Interface Sci.* **121**, 51–75 (2006).
26. Giuliano, C. B., Cvjetan, N., Ayache, J. & Walde, P. Multivesicular vesicles: preparation and applications. *ChemBioChem* **3**, e2000049 (2021).
27. Shields, C. W. IV, Reyes, C. D. & López, G. P. Microfluidic cell sorting: a review of the advances in the separation of cells from debulking to rare cell isolation. *Lab Chip* **15**, 1230–1249 (2015).
28. Benoit, M., Gabriel, D., Gerisch, G. & Gau, H. E. Discrete interactions in cell adhesion measured by single-molecule force spectroscopy. *Nat. Cell Biol.* **2**, 313–317 (2000).
29. Chu, Y. S. et al. Force measurements in E-cadherin–mediated cell doublets reveal rapid adhesion strengthened by actin cytoskeleton remodeling through Rac and Cdc42. *J. Cell Biol.* **167**, 1183–1194 (2004).
30. Maître, J. et al. Adhesion functions in cell sorting by mechanically coupling the cortices of adhering cells. *Science* **338**, 253–256 (2012).
31. Tözeren, A. et al. Micromanipulation of adhesion of a Jurkat cell to a planar bilayer membrane containing lymphocyte function-associated antigen 3 molecules. *J. Cell Biol.* **116**, 997–1006 (1992).
32. Zhao, L., Fu, X., Zhang, L. & Ye, Z. Effect of mechanical properties of Jurkat cell on adhesion properties of Jurkat integrin and VCAM-1: an AFM study. *Colloids Surf. B* **218**, 112784 (2022).
33. van der Merwe, P. A. & Barclay, A. N. Transient intercellular adhesion: the importance of weak protein-protein interactions. *Trends Biochem. Sci.* **19**, 354–358 (1994).
34. Beri, P. et al. Cell adhesiveness serves as a biophysical marker for metastatic potential. *Cancer Res.* **80**, 901–911 (2020).
35. Stroock, A. D. et al. Chaotic mixer for microchannels. *Science* **295**, 647–651 (2002).
36. Thiffeault, J.-L. Using multiscale norms to quantify mixing and transport. *Nonlinearity* **25**, R1–R44 (2012).
37. Lee, C. Y., Chang, C. L., Wang, Y. N. & Fu, L. M. Microfluidic mixing: a review. *Int. J. Mol. Sci.* **12**, 3263–3287 (2011).
38. Omar, A. K., Wu, Y., Wang, Z.-G. & Brady, J. F. Swimming to stability: structural and dynamical control via active doping. *ACS Nano* **13**, 560–572 (2019).
39. Mittasch, M. et al. Non-invasive perturbations of intracellular flow reveal physical principles of cell organization. *Nat. Cell Biol.* **20**, 344–351 (2018).
40. Wang, W. et al. Cilia metasurfaces for electronically programmable microfluidic manipulation. *Nature* **605**, 681–686 (2022).

Methods

Kinesin purification and microtubule polymerization

Kinesin purification, microtubule polymerization and chamber construction were described in previous work[11]. In short, we constructed and purified two K401 kinesins with the light-induced hetero-dimer system of iLID or SspB-micro: K401-iLID and K401-micro. For protein expression, we transformed the plasmids into BL21 pLysS cells and induced the cells with IPTG compound. For protein purification, we lysed the cells and used nickel nitrilotriacetic acid (Ni-NTA) agarose resin to pick up His-tagged proteins that were provided by the base plasmids. The maltose-binding protein (MBP) domain was used and subsequently cleaved off in K401-micro expression to ensure the micro domain remains fully functional during expression. Tubulin was polymerized with the non-hydrolysable GTP analogue GMP-CPP. Labelled and unlabelled tubulin were palleted and then incubated at 37 °C to form GMP-CPP-stabilized microtubulues. We then characterized the microtubule length distribution by immobilizing them onto a cover-glass surface using poly-L-lysine. The median microtubule length is 1.0 μm, much smaller than the critical length w_c at the scale of 100 μm (Supplementary Fig. 6).

Flow chamber treatment and construction

The chambers were made from microscope slides and cover-slips that were passivated against non-specific protein binding with a hydrophilic acrylamide coating[41]. In brief, microscope slides and cover-glass were first cleaned by sonication in 2% Hellmanex III solution for 15 min. Excess Hellmanex III was then washed out with double-distilled H_2O and then ethanol sonication. The glass was then incubated overnight in 0.1 M HCl to remove any trace metal and finished in 0.1 M KOH sonication. After cleaning and etching, the glass was immersed in a silanizing solution of 98.5% ethanol, 1% acetic acid and 0.5% 3-(trimethoxysilyl) propylmethacrylate for 10–15 min. After rinsing, the glass was baked at 110 °C for 30 min. The glass was than immersed overnight in a degassed 2% acrylamide solution with 0.035% TEMED catalyst and 3 mM ammonium persulfate. The glass was rinsed in double-distilled H_2O and air dried just before use. A flow cell made with precut parafilm was used as a seal between the microscope slides and cover-slips, making a channel that was about 70 μm in height. After the addition of reaction mixture, the flow cells were sealed with dental silicone polymer.

Energy mixture and reaction mixture

An energy mix consisting of an energy source (ATP), glycerol (which is crucial for aster formation and microtubule crosslinking in experiments, though the mechanism is not fully understood and may differ from typical macromolecular crowding effects), a surface passivating reagent (pluronic acid), oxygen scavengers (glucose oxidase, glucose, catalase, Trolox and dithiothreitol (DTT)) and ATP-recycling reagents was made on ice prior to combining the motor proteins and microtubules. After equilibrating the energy mix to ambient temperature, K401-micro, K401-iLID and microtubules were combined with the energy mix into a reaction mix. Concentrations for protein monomers for the K401-micro and K401-iLID constructs were 1 μM, and for microtubules, 1.5–2.5 μM. To minimize unintended light activation and non-specific protein binding, the sample was prepared under dark-room conditions with filters to block wavelengths below 580 nm. For all experiments conducted in this study, the reaction mixture consisted of 59.2 mM K-PIPES buffer (pH 6.1), 4.7 mM $MgCl_2$, 3.2 mM potassium chloride, 2.6 mM potassium phosphate, 0.74 mM egtazic acid (EGTA), 1.4 mM Mg ATP (Sigma A9187), 10% glycerol, 0.50 mg ml^{-1} pluronic F-127 (Sigma P2443), 0.22 mg ml^{-1} glucose oxidase (Sigma G2133), 3.2 mg ml^{-1} glucose, 0.038 mg ml^{-1} catalase (Sigma C40), 5.4 mM DTT, 2.0 mM Trolox (Sigma 238813), 0.026 units μl^{-1} pyruvate kinase/lactic dehydrogenase (Sigma P0294) and 26.6 mM phosphoenolpyruvic acid. K401-micro and K401-iLID were both diluted with a 1:2 ratio with 2 μl of M2B buffer with pH 6.1 (80 mM K-PIPES (pH 6.1), 1 mM EGTA, 2 mM $MgCl_2$). Microtubules were diluted with a 1:7 ratio with 7 μl DTT M2B with pH 6.1 (45 μl M2B (pH 6.1) with 1 μl of 250 mM DTT and 333.4 mg μl^{-1} glucose). The reaction mix was then aged in the flow cell for 120–180 min before light activation and data acquisition.

Tracer bead preparation

To visualize the fluid dynamics of our system, we used 1 μm polystyrene beads as tracer particles. The particles were incubated overnight in M2B buffer with pH 6.8 with 50 mg ml^{-1} pluronic acid. The beads were then washed and palleted at 1,000*g* for 2 min and resuspended in M2B with pH 6.8 before adding them into the reaction mix.

Fluorescent bead preparation

Fluorescent particles were used to demonstrate the mixing and transport capability of our system. We used 0.5 μm polystyrene beads that are dyed with highly hydrophobic dyes. The particles were incubated in M2B buffer with pH 6.8 with 50 mg ml^{-1} pluronic acid. The beads were then washed and palleted at 1,000*g* for 2 min and resuspended in M2B buffer with pH 6.8 before adding them into the reaction mix.

Cell culture

The cells used in the transport study (Jurkat cells, American Type Culture Collection (ATCC) TIB-152 and Raji cells, ATCC CCL-86) were cultured in a medium composed of high-glucose RPMI 1640 (Life Technologies) and 10% foetal bovine serum (qualified; Life Technologies). Jurkat cells were cultured to maintain a cell density between 1×10^5 and 3×10^6 cells ml^{-1}. Before loading the cells in the aster mix, the cells were thoroughly washed with M2B buffer with pH 6.8 (previously described in Methods). Cell cultures were first centrifuged at 300*g* for 5 min to remove the culture media, then washed twice with M2B of pH 6.8 at 300*g* for 5 min to remove any remaining culture media and salts. Subsequently, cells suspended in M2B of pH 6.8 were introduced into the microtubule buffer to attain the desired cell density. As an example, for a 5 ml culture with a density of 3×10^6 cells ml^{-1}, the typical protocol would involve suspending the cells in 1 ml of M2B with pH 6.8, of which 10 μl would be used in every 45 μl of the microtubule buffers. Raji cells were used only in Extended Data Fig. 2 because they can form larger clusters. Jurkat cells were used in Figs. 3 and 5.

Cell live/dead staining

Calcein AM (catalogue no. C1430, Life Technologies) and EthD-1 (catalogue no. E1169, Life Technologies) solutions were prepared using DMSO solvent and H_2O in a ratio of 1:4 (v/v) for a stock concentration of 1 mM. The 2 μM live/dead stain working concentration was prepared in Dulbecco's phosphate-buffered saline (DPBS; Life Technologies) by adding 20 μl of each stain to 10 ml of DPBS. Cell cultures were first centrifuged at 300*g* for 5 min to remove the culture media. The 2 μM live/dead stain was added to the cell pallet. Cells were sufficiently stained after 1 h. Cell cultures were centrifuged at 300*g* for 5 min again to remove the staining solution. Subsequently, cells were suspended in M2B with pH 6.8 and then added to the active matter mix.

Vesicle preparation

Lipid vesicles were prepared according to a modified version of the method in ref. 42. In a 15 ml glass vial, 0.5 ml chloroform was combined with 15.2 μl of 25 mg ml^{-1} 1-palmitoyl-2-oleoyl-glycero-3-phosphocholine (POPC; 850457, Avanti Polar Lipids) and 0.65 μl of 1 mg ml^{-1} dioleoyl-phosphoethanolamine-lissamine rhodamine B (rhodamine PE; 810158, Avanti Polar Lipids). The chloroform was then evaporated in a fume hood, following all safety guidelines for handling chloroform. The resulting lipid dry film was mixed with 1 ml of mineral oil (M8410, Sigma-Aldrich) to achieve a final concentration of 500 μM in oil solution. This mixture was heated to 50 °C and dissolved by pulse vortexing and sonication for 20 min. The lipid–oil mixture was stored at room temperature under dark conditions and used within two days.

Inner and outer solutions of the lipid vesicles were prepared to match the osmolarity of the active matter mix. Due to the incompatibility of our active matter system with high levels of salts or sugars, and the scarcity of the mixture itself, we increased the inner and outer solution osmolarity by adding KCl to M2B with pH 6.8 to reach 1,820 milliosmoles (mOsm), which is lower than the 2,034 mOsm of the active matter mix but does not disrupt protein functions. To form the vesicles, 300 µl of outer solution was placed in a 1.5 ml tube, and 300 µl of lipid–oil mixture was gently layered onto the outer solution. This was incubated on ice for 60 min to allow the assembly of a lipid monolayer at the interface between the oil and outer solution.

Just before use, 200 µl of lipid–oil mixture was put into a 1.5 ml sample tube and cooled on ice for >15 min. Then, 20 µl of inner solution was added to the lipid–oil mixture and immediately emulsified by first pipetting 20 times and then vortexing at maximum power (Vortex-Genie 2; Scientific Industries) for 10 s. The emulsion was incubated on ice for 5 min to stabilize by the spontaneous alignment of lipid molecules at the interface of the inner buffer and oil. Subsequently, 200 µl of the emulsion was carefully placed on the lipid–oil mixture and the outer solution, and then incubated for 5 min on ice. The 1.5 ml tube was then centrifuged (2,000*g*, 10 min, 4 °C) to push the emulsion droplets through the interface. After centrifugation, the oil layer and 500 µl of buffer solution were gently drawn off from the top of the tube.

For the final mixture, 1 µl of resuspended vesicles was added to a combination of 8 µl energy mix, 2 µl diluted iLid motor, 2 µl diluted micro motor and 1 µl diluted microtubules.

Design and implementation of different bar patterns

We custom fitted an epi-illuminated pattern projector onto our microscope. The size of the projection field was 800 × 1,280 pixels. Matrices containing coordinates of bars were first computed in Python and then converted to greyscale and eventually saved into the tagged image file format (TIFF). TIFF image sequences were then processed by a custom Micro-Manager script. The scripts can be found at https://github.com/fy26/ActiveMatter.

Data acquisition and projection of patterns

All experiments were performed with an automated wide-field epifluorescence microscope with a custom epi-illuminated projector and gated light-emitting diode (LED) transmitted light, as discussed in our previous work[11]. All samples were imaged at ×10 magnification. Image sequences were captured using a Nikon TI2 controlled with Micro-Manager. Images of the fluorescent microtubules (Cy5 dye) and tracer particles (bright field) were acquired every 8 s. Bar patterns were projected onto the image plane every 8 s with a brief 200 ms flash of a 2.4 mW mm^{-2} activation light from a 470 nm LED.

Duration of the activation light

The duration of the light was empirically determined through an iterative process: (1) We started with a short activation time, such as 50 ms, and gradually increased it in 50 ms increments. (2) After each increment, we observed the sample for aster formation. (3) We continued steps 1 and 2 until we observed the formation of a stable aster, defining this as the optimal activation time. (4) A longer pulse duration resulted in contractile activity outside of the intended light pattern, helping establish an upper limit for the activation duration.

Particle image velocimetry

Particle image velocimetry was performed on the images of tracer beads using PIVlab[43,44] to extract the solvent flow fields.

Derivation of the general principle for linear superposition

The generalized Stokes equation for the solvent flow is $\mathbf{f} + \mu\nabla^2\mathbf{u} - \nabla p = \mathbf{0}$, where $\mathbf{f}$ is the body force applied by external fields or sources; for example, in our system the body force is from the active force generated by the crosslinked microtubules and motors. We now construct a general principle for the linear superposition of flows induced by n different force-generating sources. We denote the force applied on the fluid from the source i, in the absence of other sources, as $\mathbf{f}_i$, and the resultant flow and pressure fields as $\mathbf{u}_i$ and p_i, respectively. Similarly, the body force, flow field and pressure field in the presence of all the n sources are denoted by $\mathbf{f}_t$, $\mathbf{u}_t$ and p_t, respectively. To establish a linear regime of fluid flows driven by different sources, we require $\mathbf{u}_t = \sum_i \mathbf{u}_i$ and $p_t = \sum_i p_i$, which can be substituted into the Stokes equation and yields $\mathbf{f}_t = \sum_i \mathbf{f}_i$. This result directly comes from the linearity of the Stokes equation in $\mathbf{u}$ and p; however, it is not trivial because $\mathbf{f}_i$ can depend on the flow velocity $\mathbf{u}$, and the formula $\mathbf{f}_t = \sum_i \mathbf{f}_i$ does not always hold. In our system, the force-generating sources are the microtubule networks, and the force induced by a single network i, in the absence of all other networks, can be expressed as $\mathbf{f}_i = \gamma c_i(\mathbf{v}_i - \mathbf{u}_i)$, where γ is the drag coefficient of the microtubule and the solvent, and c and $\mathbf{v}$ are the density and velocity of the microtubule network, respectively. Therefore, in the presence of n networks, the general principle $\mathbf{f}_t = \sum_i \mathbf{f}_i$ together with the additional linear relationships, $c_t = \sum_i c_i$ and $\mathbf{v}_t = \sum_i \mathbf{v}_i$, requires that $\sum_i c_i \cdot \sum_j \mathbf{v}_j = \sum_i c_i \mathbf{v}_i$ and $\sum_i c_i \cdot \sum_j \mathbf{u}_j = \sum_i c_i \mathbf{u}_i$. The former requires that $c_i \mathbf{v}_j = \mathbf{0}$ when $i \neq j$, which is automatically satisfied as long as no networks overlap in the system. The latter requires that $c_i \mathbf{u}_j = 0$ for any $i \neq j$, which is the rule of linear superposition in a multiple-active-agent system.

Numerical simulation

The finite difference method was used in numerical simulations, with the central differencing scheme in space and the method of lines in time. The codes are written in Python and available at https://github.com/fy26/ActiveMatter/tree/main/Simulation.

Calculation of shear modulus

The steady-state value of DF depends on the capillary number $\mathrm{Ca} = \mu \frac{\partial u_x}{\partial x} R/G$ (refs. 45–47), where R is the radius of the aster and G is the shear modulus, via a linear relationship $\mathrm{DF} = A\mathrm{Ca}$. The value of coefficient A is calculated to be 25/6 for elastic capsules[45,47], and measured to be around 20 for viscoelastic drops[46]. Here we choose $A = 10$ to estimate the shear modulus G of the microtubule aster. Additionally using measurements $\mu = 0.02$ Pa s (ref. 48), $\partial u_x/\partial x = 0.0015\ \mathrm{s}^{-1}$, $R = 100$ µm, $L = 120$ µm and $B = 70$ µm, the shear modulus G of the aster is calculated to be 1×10^{-7} Pa.

Calculation of detachment force on cells in an extensional flow

The flow-induced friction $\mathbf{f}_p$ on a spherical particle translating in an unbounded fluid with velocity $\mathbf{v}$ is $\mathbf{f}_p = -6\pi\mu a\mathbf{v}$, which is used to approximate the force on detaching cells. We denote the two attached cells by a and b, and the unperturbed flow velocity at the two cell centres by $\mathbf{u}_a$ and $\mathbf{u}_b$, respectively. Then the cell pair moves at the same velocity $(\mathbf{u}_a + \mathbf{u}_b)/2$. The magnitude of the flow-induced force on each cell is $\mathbf{f}_p = 3\pi\mu a|\mathbf{u}_a - \mathbf{u}_b| = 3\pi\mu a|\partial\mathbf{u}/\partial x|\Delta l$. The detachment force on each cell has the same magnitude as $\mathbf{f}_p$.

Reporting summary

Further information on research design is available in the Nature Portfolio Reporting Summary linked to this article.

Data availability

All data are publicly available at https://data.caltech.edu/records/xkdvq-9r805.

Code availability

The simulation code is available on GitHub at https://github.com/fy26/ActiveMatter/tree/main/Simulation. The code for data analysis is available at https://data.caltech.edu/records/xkdvq-9r805. The Java scripts used to run Micro-Manager for imaging data collection

are deposited at https://github.com/fy26/ActiveMatter/tree/main/Micromanager%20script.

References

41. Lau, A. W. C., Prasad, A. & Dogic, Z. Condensation of isolated semi-flexible filaments driven by depletion interactions. *EPL* **87**, 48006 (2009).
42. Noireaux, V. & Libchaber, A. A vesicle bioreactor as a step toward an artificial cell assembly. *Proc. Natl Acad. Sci. USA* **101**, 17669–17674 (2004).
43. Thielicke, W. & Stamhuis, E. J. PIVlab – towards user-friendly, affordable and accurate digital particle image velocimetry in MATLAB. *J. Open Res. Softw.* **2**, e30 (2014).
44. Thielicke, W. & Sonntag, R. Particle image velocimetry for MATLAB: accuracy and enhanced algorithms in PIVlab. *J. Open Res. Softw.* **9**, 12 (2021).
45. Lac, E., Barthés-Biesel, D., Pelekasis, N. A. & Tsamopoulos, J. Spherical capsules in three-dimensional unbounded Stokes flows: effect of the membrane constitutive law and onset of buckling. *J. Fluid Mech.* **516**, 303–334 (2004).
46. Hsu, A. S. & Leal, L. G. Deformation of a viscoelastic drop in planar extensional flows of a Newtonian fluid. *J. Non-Newton. Fluid Mech.* **160**, 176–180 (2009).
47. de Loubens, C. et al. Mechanical characterization of cross-linked serum albumin microcapsules. *Soft Matter* **10**, 4561–4568 (2014).
48. Gagnon, D. A. et al. Shear-induced gelation of self-yielding active networks. *Phys. Rev. Lett.* **125**, 178003 (2020).

Acknowledgements

We thank J. Wang, D. Larios and J. Brady for fruitful discussions. We are also grateful to H. A. Stone, Z. Gartner, A. Liu and A. Lourenço for valuable advice on the paper. We thank I.-M. Strazhnik for preparing the figures and proofreading the text. This work is funded by the Packard Foundation, Moore Foundation, National Institutes of Health and Donna and Benjamin M. Rosen Bioengineering Center. F.Y. acknowledges support from a BBE Divisional Fellowship at Caltech. R.P. acknowledges the National Institutes of Health 1R35 GM118043 award (Maximizing Investigators' Research Award).

Author contributions

M.T. supervised the project. M.T., F.Y. and S.L. designed the study. S.L. and H.J.L. conducted the experiments. F.Y. conducted preliminary experiments. F.Y. and S.L. analysed the experimental data. F.Y. derived the model and performed the numerical simulations. H.J.L. and R.P. contributed to the technical expertise, materials and discussion. F.Y., M.T. and S.L. wrote the paper. All authors revised the completed paper.

Competing interests

The authors declare no competing interests.

Additional information

Extended data is available for this paper at https://doi.org/10.1038/s41563-024-02090-w.

Supplementary information The online version contains supplementary material available at https://doi.org/10.1038/s41563-024-02090-w.

Correspondence and requests for materials should be addressed to Fan Yang or Matt Thomson.

Peer review information *Nature Materials* thanks Makito Miyazaki and the other, anonymous, reviewer(s) for their contribution to the peer review of this work.

https://doi.org/10.1038/s41563-024-02090-w

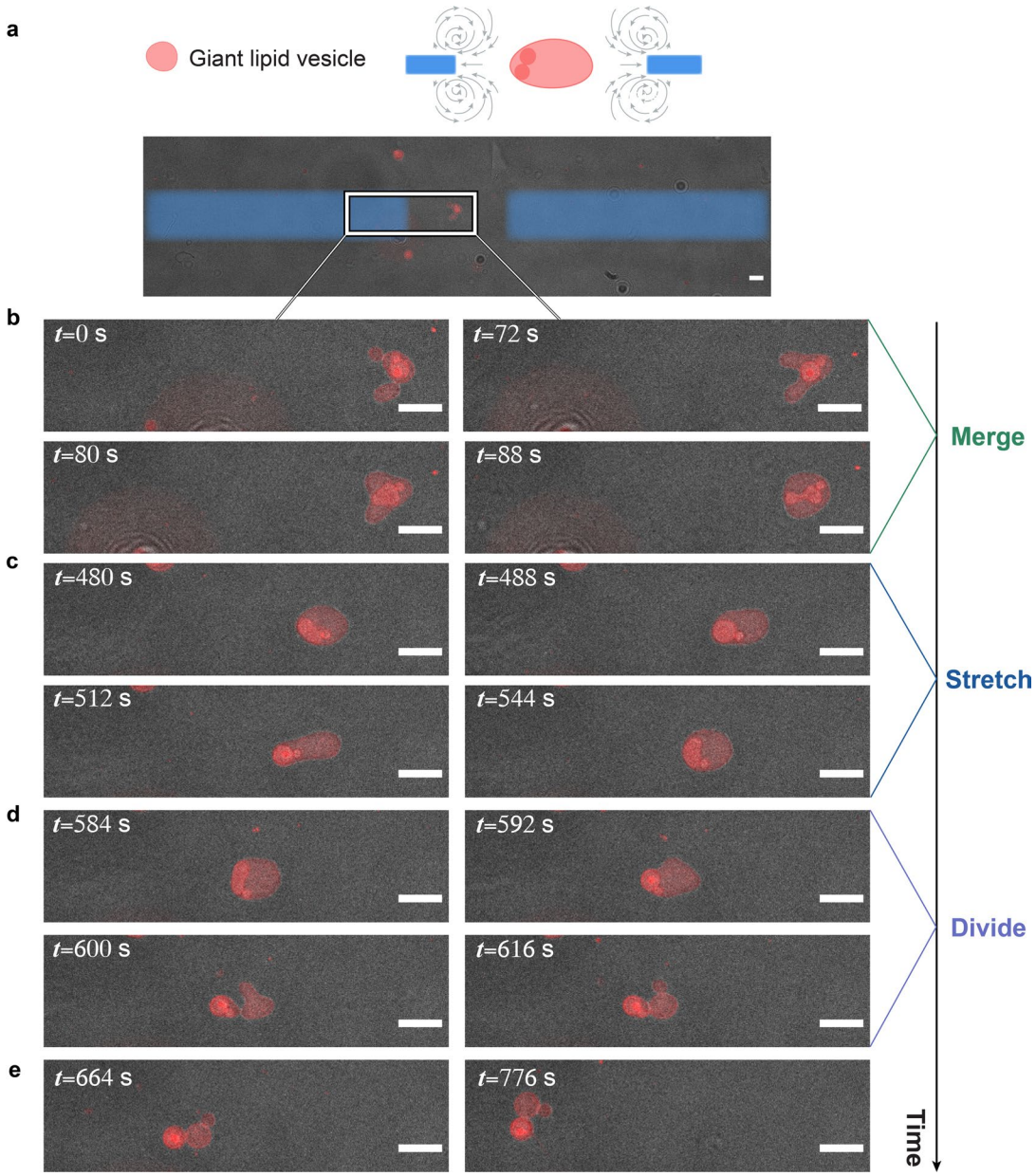

Extended Data Fig. 1 | The stretching module can stretch and divide a giant lipid vesicle (GV) into daughter vesicles. a, Sketch of the experimental setup. The GVs are dyed red. **b**, 3 GVs merge into a single GV. **c**, The fused GV is stretched along the horizontal direction. **d**, The fused GV is divided into 3 daughter vesicles. **e**, The daughter vesicles are stable. Scale bars, 20 μm.

https://doi.org/10.1038/s41563-024-02090-w

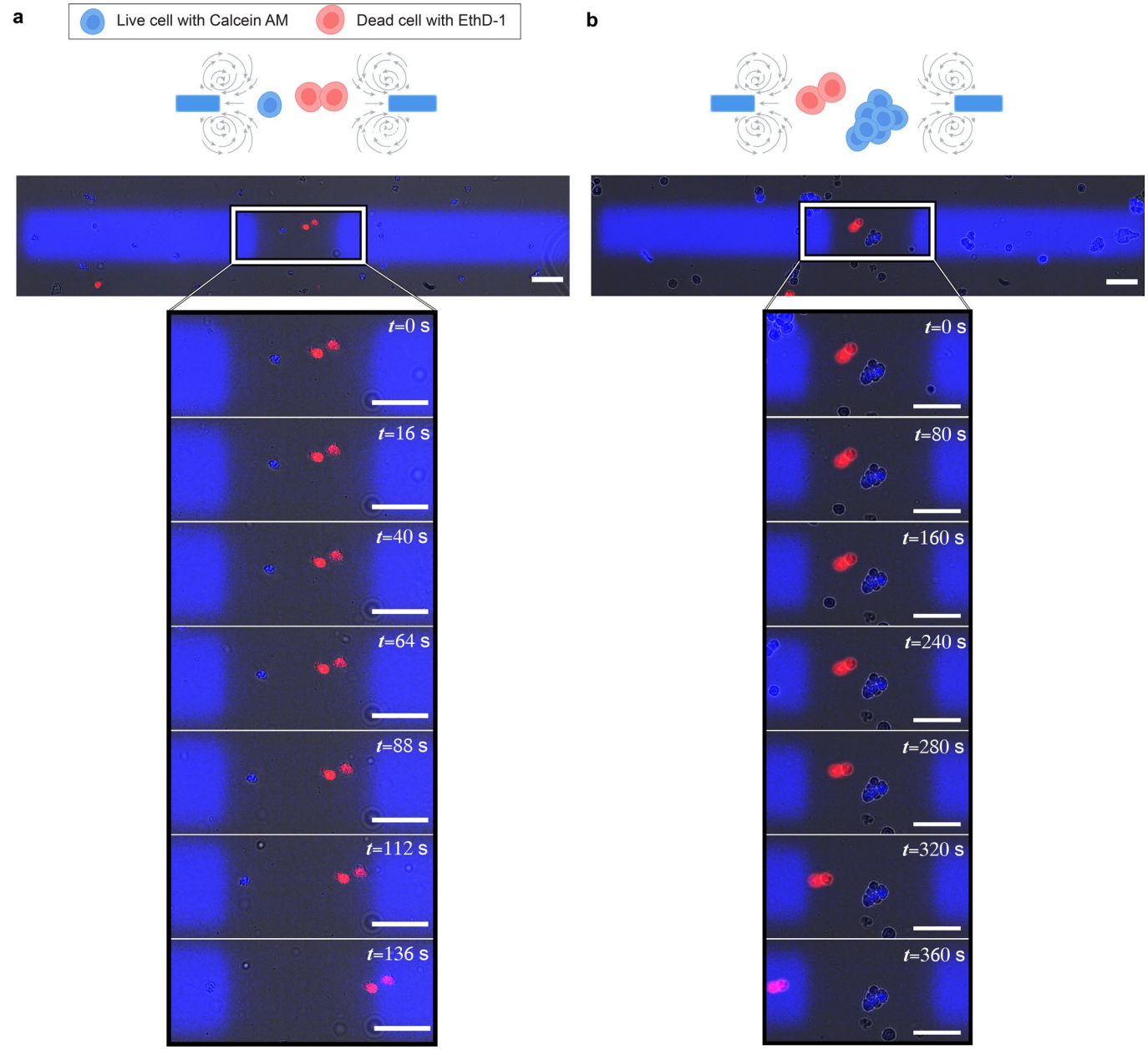

Extended Data Fig. 2 | The stretching module can isolate dead cells (red) from live cells (blue). a, Time-lapse images of isolating one live cell from a pair of dead cells. **b**, Time-lapse images of isolating a dead-cell pair from a live-cell cluster, without disturbing the latter. Raji cells (Methods) are used in this figure because they can form large clusters.

nature portfolio

Corresponding author(s): Matt Thomson and Fan Yang

Last updated by author(s): Nov 5, 2024

Reporting Summary

Nature Portfolio wishes to improve the reproducibility of the work that we publish. This form provides structure for consistency and transparency in reporting. For further information on Nature Portfolio policies, see our Editorial Policies and the Editorial Policy Checklist.

Statistics

For all statistical analyses, confirm that the following items are present in the figure legend, table legend, main text, or Methods section.

n/a	Confirmed	
☐	☒	The exact sample size (*n*) for each experimental group/condition, given as a discrete number and unit of measurement
☒	☐	A statement on whether measurements were taken from distinct samples or whether the same sample was measured repeatedly
☒	☐	The statistical test(s) used AND whether they are one- or two-sided *Only common tests should be described solely by name; describe more complex techniques in the Methods section.*
☒	☐	A description of all covariates tested
☒	☐	A description of any assumptions or corrections, such as tests of normality and adjustment for multiple comparisons
☐	☒	A full description of the statistical parameters including central tendency (e.g. means) or other basic estimates (e.g. regression coefficient) AND variation (e.g. standard deviation) or associated estimates of uncertainty (e.g. confidence intervals)
☒	☐	For null hypothesis testing, the test statistic (e.g. *F*, *t*, *r*) with confidence intervals, effect sizes, degrees of freedom and *P* value noted *Give P values as exact values whenever suitable.*
☒	☐	For Bayesian analysis, information on the choice of priors and Markov chain Monte Carlo settings
☒	☐	For hierarchical and complex designs, identification of the appropriate level for tests and full reporting of outcomes
☒	☐	Estimates of effect sizes (e.g. Cohen's *d*, Pearson's *r*), indicating how they were calculated

Our web collection on statistics for biologists contains articles on many of the points above.

Software and code

Policy information about availability of computer code

Data collection	Imaging data was collected using Micro-Manager 1.4.21. Image projection code was written in Beanshll, a Java source interpreter built-in with Micro-Manager 1.x API and deployed using the script manager function in Micro-Manager. Java scripts are deposited at https://github.com/fy26/ActiveMatter/tree/main/Micromanager%20script. Ti2_Mic_Driver.dll from Ti2 Control 1.2.0, and mmgr_dal_HamamatsuHam.dll from Micro-Manager were used for controlling the microscope and the camera.
Data analysis	PIVlab (v 2.53) was used to measure the flow fields. Data analysis was performed in Python 3.9 and the code has been deposited in the Caltech Data at https://data.caltech.edu/records/xkdvq-9r805.

For manuscripts utilizing custom algorithms or software that are central to the research but not yet described in published literature, software must be made available to editors and reviewers. We strongly encourage code deposition in a community repository (e.g. GitHub). See the Nature Portfolio guidelines for submitting code & software for further information.

Data

Policy information about availability of data

All manuscripts must include a data availability statement. This statement should provide the following information, where applicable:

- Accession codes, unique identifiers, or web links for publicly available datasets
- A description of any restrictions on data availability
- For clinical datasets or third party data, please ensure that the statement adheres to our policy

All data are publicly available in the Caltech Data at https://data.caltech.edu/records/xkdvq-9r805.

Research involving human participants, their data, or biological material

Policy information about studies with human participants or human data. See also policy information about sex, gender (identity/presentation), and sexual orientation and race, ethnicity and racism.

Reporting on sex and gender	No human participants were involved in this study.
Reporting on race, ethnicity, or other socially relevant groupings	No human participants were involved in this study.
Population characteristics	No human participants were involved in this study.
Recruitment	No human participants were involved in this study.
Ethics oversight	No human participants were involved in this study.

Note that full information on the approval of the study protocol must also be provided in the manuscript.

Field-specific reporting

Please select the one below that is the best fit for your research. If you are not sure, read the appropriate sections before making your selection.

☒ Life sciences ☐ Behavioural & social sciences ☐ Ecological, evolutionary & environmental sciences

For a reference copy of the document with all sections, see nature.com/documents/nr-reporting-summary-flat.pdf

Life sciences study design

All studies must disclose on these points even when the disclosure is negative.

Sample size	Experiments were repeated approximately 5 times. Specific details on the number of samples are provided in the manuscript for each experiments.
Data exclusions	No data were excluded from analysis.
Replication	Experiments were repeated approximately 5 times to ensure reproducibility and to average out noise due to batch effects. Each replication used freshly prepared reagents. Additionally, four different batches of materials were used to verify consistency across different preparations. During the review process, experiments were repeated using different batches of materials and cells, successfully reproducing the original data.
Randomization	Randomization is not required in this study as the samples are not separated into different groups.
Blinding	Blinding is not required as there is no sample group allocation.

Reporting for specific materials, systems and methods

We require information from authors about some types of materials, experimental systems and methods used in many studies. Here, indicate whether each material, system or method listed is relevant to your study. If you are not sure if a list item applies to your research, read the appropriate section before selecting a response.

Materials & experimental systems

n/a	Involved in the study
☒	☐ Antibodies
☐	☒ Eukaryotic cell lines
☒	☐ Palaeontology and archaeology
☒	☐ Animals and other organisms
☒	☐ Clinical data
☒	☐ Dual use research of concern
☒	☐ Plants

Methods

n/a	Involved in the study
☒	☐ ChIP-seq
☒	☐ Flow cytometry
☒	☐ MRI-based neuroimaging

Eukaryotic cell lines

Policy information about cell lines and Sex and Gender in Research

Cell line source(s)	Raji cells were sourced from ATCC (cat# CCL-86). The Raji line of lymphoblast-like cells was established by R.J.V. Pulvertaft in 1963 from a Burkitt's lymphoma of the left maxilla of an 11-year-old Black male. Jurkat cells were sourced from ATCC (cat# TIB-152). The Jurkat cell line was established from the peripheral blood of a 14 year old boy by Schneider et al., and was originally designated JM.
Authentication	Neither of the cell lines were authenticated.
Mycoplasma contamination	Neither of the cell lines were checked for mycoplasma contamination.
Commonly misidentified lines (See ICLAC register)	No commonly misidentified lines were used in this study.

Plants

Seed stocks	*Report on the source of all seed stocks or other plant material used. If applicable, state the seed stock centre and catalogue number. If plant specimens were collected from the field, describe the collection location, date and sampling procedures.*
Novel plant genotypes	*Describe the methods by which all novel plant genotypes were produced. This includes those generated by transgenic approaches, gene editing, chemical/radiation-based mutagenesis and hybridization. For transgenic lines, describe the transformation method, the number of independent lines analyzed and the generation upon which experiments were performed. For gene-edited lines, describe the editor used, the endogenous sequence targeted for editing, the targeting guide RNA sequence (if applicable) and how the editor was applied.*
Authentication	*Describe any authentication procedures for each seed stock used or novel genotype generated. Describe any experiments used to assess the effect of a mutation and, where applicable, how potential secondary effects (e.g. second site T-DNA insertions, mosiacism, off-target gene editing) were examined.*